

A variational discrete element method for the computation of Cosserat elasticity

Frédéric Marazzato

Department of Mathematics, Louisiana State University, Baton Rouge, LA 70803, USA
email: marazzato@lsu.edu

August 21, 2022

Abstract

The variational discrete element method developed in [18] for dynamic elastoplastic computations is adapted to compute the dynamic evolution of elastic Cosserat materials. In addition to cellwise displacement degrees of freedom (dofs), cellwise rotational dofs are added. A reconstruction is devised to obtain P^1 non-conforming polynomials in each cell and thus constant strains and stresses in each cell. The method requires only the usual macroscopic parameters of a Cosserat material and no microscopic parameter. The mass matrix is naturally diagonal and thus allows fast dynamic computations. Numerical examples show the robustness of the method and that it converges at order one in energy norm similarly to the usual Lagrange P^2 - P^1 mixed element. Also, the robustness of the method with respect to the incompressible limit $\nu \rightarrow 0.5$ is proved numerically.

1 Introduction

Cosserat continua have been introduced in [8]. They generalize Cauchy continua by adding a microscopic rotation to every infinitesimal element. Cauchy continua can be considered as a generalization of Timoshenko beams to two and three-dimensional structures. Contrarily to traditional Cauchy continua of order one, Cosserat continua are able to reproduce some effects of the micro-structure of a material through the definition of a characteristic length written ℓ . In [13], the authors design a homogenisation scheme depending on the relative size of ℓ with respect to the characteristic size L of the structure considered. Cosserat media can appear as homogenization of masonry structures [32, 14]. Cosserat media have also been used to model liquid crystals [11] and Bingham–Cosserat fluids [31], for instance. Cosserat continua are also used in rock mechanics to model localization in faults under shear deformation [28].

Discrete Element methods have been introduced in [15] to model crystalline materials and in [9] for applications to geotechnical problems. Their use in granular materials and rock simulation is still widespread [26, 29]. Although DEM are able to represent accurately the behaviour of granular materials, their use to compute elastic materials is more delicate especially regarding the choice of microscopic material parameters [16]. To remedy this problem couplings of DEM with Finite Element Methods (FEM) have been devised [19]. DEM-FEM couplings can also be used to simulate particle flows [4]. Beyond DEM-FEM couplings, attempts to simulate continuous materials with DEM have been proposed. In [2], the authors used a stress reconstruction inspired by statistical physics

but the method suffers from the non-convergence of the macroscopic parameters with respect to the microscopic parameters. In [25] the authors derive a DEM method from a Lagrange P^1 FEM but cannot simulate materials with $\nu \geq 0.3$. In [21], the authors pose the basis of variational DEM by deriving forces from potentials and link their method to Cosserat continua. Following this work, [18] proposed a variational DEM that can use polyhedral meshes and which is a full discretization of dynamic elasto-plasticity equations for a Cauchy continua. The method is also robust with respect to the incompressible limit $\nu \rightarrow 0.5$. The present paper builds on these achievements by adding cellwise rotational degrees of freedom (dofs) to take into account micro-rotations. Using the proposed method allows to use the usual tools of FEM applied to a DEM and thus makes its use and analysis much easier. Also, the possibility to use tetrahedral meshes lightens the procedure as their production is much easier than Voronoi meshes which are used in [21, 1]. Cosserat elasticity is usually computed through a P^2 - P^1 Lagrange mixed element [27]. Unfortunately, this element is not robust with respect to the incompressible limit $\nu \rightarrow 0.5$ and suffers from numerical locking. The proposed methods does not.

In the present method, displacement and rotational dofs are placed at the barycentre of every cell and the Dirichlet boundary conditions are imposed weakly similarly to discontinuous Galerkin methods [3]. The convergence rate of the method is similar to the mixed P^2 - P^1 element [27] which is one in energy norm. However, the coupling with a classical DEM is much easier due to the presence of cell dofs only.

The general elasto-dynamic problem in a Cosserat continuum is presented in Section 2. The discrete setting is then presented in Section 3 and alongside in Section 3.6, the discrete strain-stress system derived from the continuous equations is reinterpreted in a DEM fashion as a force-displacement system. In Section 4, 2d and 3d numerical tests are performed and prove the robustness and the precision of the chosen approach. Finally, Section 5 draws some conclusions and presents potential subsequent work.

2 Governing equations

An elastic material occupying, in the reference configuration, the domain $\Omega \subset \mathbb{R}^d$, where $d = 2, 3$, is considered to evolve dynamically over the time-interval $(0, T)$, where $T > 0$, under the action of volumetric forces and boundary conditions. The strain regime is limited to small strains and the material is supposed to have a micro-structure responding to a Cosserat material law. The material is also supposed to be isotropic and homogeneous. The displacement field is written $u \in \mathbb{R}^3$ and the rotation $R \in SO_3(\mathbb{R})$. Under the small strain regime, the rotation R can be mapped to a micro-rotation $\varphi \in \mathbb{R}^3$ such that $\varphi = -\frac{1}{2}\epsilon : R$ and $R = \mathbf{1} - \epsilon \cdot \varphi$, where $\mathbf{1}$ is the unit three dimensional tensor and ϵ is a third-order tensor giving the signature of a permutation (i, j, k) . Thus $\epsilon_{ijk} = 1$ for an even permutation, -1 for an odd permutation and 0 , otherwise. For instance $\epsilon_{123} = 1$, $\epsilon_{112} = 0$ and $\epsilon_{132} = -1$.

Remark 1 (2d case). *In two space dimensions, the micro-rotation is just a scalar $\varphi \in \mathbb{R}$.*

The deformation tensor e and the tension-curvature tensor κ are defined as

$$\begin{cases} e(u, \varphi) = \nabla u + \epsilon \cdot \varphi \\ \kappa(\varphi) = \nabla \varphi \end{cases} \quad (1)$$

The force-stress tensor σ and the couple-stress tensor μ are linked to the strains (e, κ) by

$$\begin{cases} \sigma(u, \varphi) = \mathbb{C} : e(u, \varphi) \\ \mu(\varphi) = \mathbb{D} : \kappa(\varphi), \end{cases} \quad (2)$$

where \mathbb{C} and \mathbb{D} are fourth-order tensors translating the material behaviour. Note that $\sigma(u, \varphi)$ is generally not symmetric unlike in Cauchy continua. We write:

$$\begin{aligned}\sigma(u, \varphi) &= K \operatorname{tr}(e)(u, \varphi) \mathbf{1} + 2G \left(\operatorname{Sym}(e)(u, \varphi) - \frac{1}{d} \operatorname{tr}(e)(u, \varphi) \mathbf{1} \right) + 2G_c \operatorname{Skew}(e)(u, \varphi), \\ \mu(\varphi) &= L \operatorname{tr}(\kappa)(\varphi) \mathbf{1} + 2M \left(\operatorname{Sym}(\kappa)(\varphi) - \frac{1}{d} \operatorname{tr}(\kappa)(\varphi) \mathbf{1} \right) + 2M_c \operatorname{Skew}(\kappa)(\varphi),\end{aligned}\tag{3}$$

where K, G, G_c, L, M and M_c are elastic moduli and Sym gives the symmetric part of a rank-two tensor whereas Skew gives its skew-symmetric part. Under supplementary assumptions, the number of elastic moduli can be reduced from six to four in three dimensions [17] but that is not the path chosen in this paper.

Remark 2 (2d case). *When $d = 2$, one only has $\mu(\varphi) = M\kappa(\varphi)$ and thus $L = M_c = 0$.*

Following [13], a characteristic length ℓ can be defined in a Cosserat elastic medium as $\max_{ijkl} \mathbb{C}_{ijkl} = \ell^2 (\max_{ijkl} \mathbb{D}_{ijkl})$. However, to have a definition of ℓ robust with respect to the incompressible limit $K \rightarrow +\infty$, we choose $\ell^2 := \frac{M}{G}$. We introduce the volumic mass $\rho \in \mathbb{R}$ and $I \in \mathbb{R}^{3 \times 3}$ is the micro-inertia tensor. The dynamics equation in strong form write

$$\begin{cases} \operatorname{div}(\sigma(u, \varphi)) + f = \rho \ddot{u} \\ \operatorname{div}(\mu(\varphi)) - \epsilon : \sigma(u, \varphi) + \mathbf{c} = \rho I \cdot \ddot{\varphi}. \end{cases}\tag{4}$$

Let $\partial\Omega = \partial\Omega_N \cup \partial\Omega_D$ be a partition of the boundary of Ω . By convention $\partial\Omega_D$ is a closed set and $\partial\Omega_N$ is a relatively open set in $\partial\Omega$. The boundary $\partial\Omega_D$ has imposed displacement and micro-rotation (u_D, φ_D) , we thus enforce

$$\begin{cases} u = u_D \text{ on } \partial\Omega_D, \\ \varphi = \varphi_D \text{ on } \partial\Omega_D. \end{cases}\tag{5}$$

The normal and couple stresses (g, m) are imposed on $\partial\Omega_N$, that is, we enforce

$$\begin{cases} \sigma \cdot n = g \text{ on } \partial\Omega_N, \\ \mu \cdot n = m \text{ on } \partial\Omega_N. \end{cases}\tag{6}$$

To write a variational DEM, we write the dynamics equations in weak form. Taking $(\tilde{u}, \tilde{\varphi})$ as test functions, verifying homogeneous Dirichlet boundary conditions on $\partial\Omega_D$ ($\tilde{u}|_{\partial\Omega_D} = 0 = \tilde{\varphi}|_{\partial\Omega_D}$), one has over $(0, T)$

$$\begin{aligned} \int_{\Omega} \rho \ddot{u} \cdot v + \rho (I \cdot \ddot{\varphi}) \cdot \psi + \int_{\Omega} e(u, \varphi) : \mathbb{C} : e(v, \psi) + \kappa(\varphi) : \mathbb{D} : \kappa(\psi) \\ = \int_{\Omega} f \cdot v + \mathbf{c} \cdot \psi + \int_{\partial\Omega_N} g \cdot v + m \cdot \psi, \end{aligned}\tag{7}$$

while still imposing the Dirichlet boundary conditions of Equation (5). Note that the bilinear form in the left-hand side of (7) is symmetric.

3 Space semidiscretization

The domain Ω is discretized with a mesh \mathcal{T}_h of size h made of polyhedra with planar facets in three space dimensions or polygons with straight edges in two space dimensions. We assume that Ω is itself a polyhedron or a polygon so that the mesh covers Ω exactly, and we also assume that the mesh is compatible with the partition of the boundary $\partial\Omega$ into the Dirichlet and Neumann parts.

3.1 Degrees of freedom

Let \mathcal{C} denote the set of mesh cells. Pairs of vector-valued volumetric degrees of freedom (dofs) for a generic displacement field and a generic micro-rotation field $(v_h, \psi_h) := (v_c, \psi_c)_{c \in \mathcal{C}} \in \mathbb{R}^{2d\#(\mathcal{C})}$ are placed at the barycentre of every mesh cell $c \in \mathcal{C}$, where $\#(S)$ denotes the cardinality of any set S . Figure 1 illustrates the position of the dofs in the mesh.

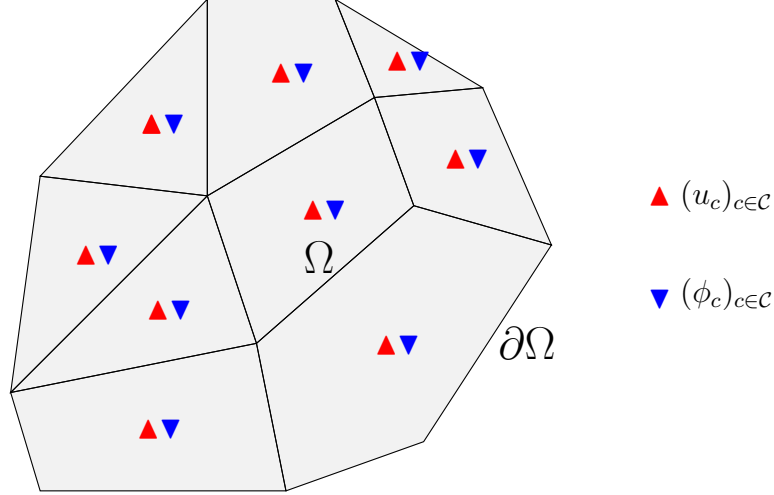


Figure 1: Continuum Ω covered by a polyhedral mesh and vector-valued degrees of freedom for the displacement.

Let \mathcal{F} denote the set of mesh facets. We partition this set as $\mathcal{F} = \mathcal{F}^i \cup \mathcal{F}^b$, where \mathcal{F}^i is the collection of the internal facets shared by two mesh cells and \mathcal{F}^b is the collection of the boundary facets sitting on the boundary $\partial\Omega$ (such facets belong to the boundary of only one mesh cell). The sets \mathcal{F}_N^b and \mathcal{F}_D^b are defined as a partition of \mathcal{F}^b such that $\forall F \in \mathcal{F}_N^b, F \subset \partial\Omega_N$ and $\forall F \in \mathcal{F}_D^b, F \subset \partial\Omega_D$.

3.2 Facet reconstructions

Using the cell dofs introduced above, we reconstruct a collection of displacements and micro-rotations $(v_{\mathcal{F}}, \psi_{\mathcal{F}}) := (v_F, \psi_F)_{F \in \mathcal{F}} \in \mathbb{R}^{2d\#(\mathcal{F})}$ on the mesh facets. The facet reconstruction operator is denoted \mathcal{R} and we write

$$(v_{\mathcal{F}}, \psi_{\mathcal{F}}) := (\mathcal{R}(v_h), \mathcal{R}(\psi_h)). \quad (8)$$

The reconstruction operator \mathcal{R} is constructed in the same way as in the finite volume methods studied in [12, Sec. 2.2] and the variational DEM developed in [18]. For a given facet $F \in \mathcal{F}$, we select neighbouring cells collected in a subset denoted \mathcal{C}_F , as well as coefficients $(\alpha_F^c)_{c \in \mathcal{C}_F}$ and we set

$$\begin{cases} \mathcal{R}_F(v_h) := \sum_{c \in \mathcal{C}_F} \alpha_F^c v_c, & \forall v_h \in V_h, \\ \mathcal{R}_F(\psi_h) := \sum_{c \in \mathcal{C}_F} \alpha_F^c \psi_c, & \forall \psi_h \in V_h. \end{cases} \quad (9)$$

The reconstruction is based on barycentric coordinates. The coefficients α_F^c are chosen as the barycentric coordinates of the facet barycentre \mathbf{x}_F in terms of the location of the

barycenters of the cells in \mathcal{C}_F . For any facet $F \in \mathcal{F}$, the set \mathcal{C}_F is constructed so as to contain exactly $(d + 1)$ points forming the vertices of a non-degenerate simplex. Thus, the barycentric coefficients $(\alpha_F^c)_{c \in \mathcal{C}_F}$ are computed by solving the linear system:

$$\begin{cases} \sum_{c \in \mathcal{C}_F} \alpha_F^c = 1, & \forall F \in \mathcal{F}, \\ \sum_{c \in \mathcal{C}_F} \alpha_F^c \mathbf{x}_c = \mathbf{x}_F, & \forall F \in \mathcal{F}, \end{cases} \quad (10)$$

where \mathbf{x}_c is the position of the barycenter of the cell c . An algorithm is presented thereafter to explain the selection of the neighbouring dofs in \mathcal{C}_F . This algorithm has to be viewed more as a proof-of-concept than as an optimized algorithm. For a more involved algorithm, see [18]. We observe that this algorithm is only used in a preprocessing stage of the computations. For a given facet $F \in \mathcal{F}$,

1. Assemble in a set \mathcal{N}_F the cell or cells containing the facet F . Then, add to \mathcal{N}_F the cells sharing a facet with the cells already in \mathcal{N}_F . Repeat one last time this last operation.
2. Select a subset \mathcal{C}_F of \mathcal{N}_F with exactly $(d + 1)$ elements and whose cell barycenters form a non-degenerate simplex (tetrahedron in 3d and triangle in 2d).

This algorithm ensures that the dofs selected for the reconstruction in Equation (9) remain $\mathcal{O}(h)$ close to the facet F .

3.3 Gradient reconstruction

Using the reconstructed facet displacements and micro-rotations and a discrete Stokes formula, it is possible to devise a discrete $\mathbb{R}^{d \times d}$ -valued piecewise-constant gradient field for the displacement and the micro-rotation that we write $\mathcal{G}_c(v_{\mathcal{F}}) := (\mathcal{G}_c(v_{\mathcal{F}}))_{c \in \mathcal{C}} \in \mathbb{R}^{d^2 \#(\mathcal{C})}$ and $\mathcal{G}_c(\psi_{\mathcal{F}}) := (\mathcal{G}_c(\psi_{\mathcal{F}}))_{c \in \mathcal{C}} \in \mathbb{R}^{d^2 \#(\mathcal{C})}$. Specifically we set in every mesh cell $c \in \mathcal{C}$,

$$\begin{cases} \mathcal{G}_c(v_{\mathcal{F}}) := \sum_{F \in \partial c} \frac{|F|}{|c|} v_F \otimes n_{F,c}, & \forall v_{\mathcal{F}} \in \mathbb{R}^{d \#(\mathcal{F})}, \\ \mathcal{G}_c(\psi_{\mathcal{F}}) := \sum_{F \in \partial c} \frac{|F|}{|c|} \psi_F \otimes n_{F,c}, & \forall \psi_{\mathcal{F}} \in \mathbb{R}^{d \#(\mathcal{F})}, \end{cases} \quad (11)$$

where the summation is over the facets F of c and $n_{F,c}$ is the outward normal to c on F . Consequently, the strains are defined for $c \in \mathcal{C}$ as

$$\begin{cases} e_c(v_h) := \mathcal{G}_c(v_h) + \epsilon \cdot \psi_c \in \mathbb{R}^{d \times d}, \\ \kappa_c(\psi_h) := \mathcal{G}_c(\psi_h) \in \mathbb{R}^{d \times d}, \end{cases} \quad (12)$$

where $\mathcal{G}_c(v_h) := \mathcal{G}_c(\mathcal{R}(v_h))$ and $\mathcal{G}_c(\psi_h) := \mathcal{G}_c(\mathcal{R}(\psi_h))$. Consequently, the discrete bilinear form of elastic energies writes

$$a_{\text{elas}}((u_h, \varphi_h); (v_h, \psi_h)) := \int_{\Omega} (e_h((u_h, \varphi_h)) : \mathbb{C} : e_h((v_h, \psi_h)) + \kappa_h(\varphi_h) : \mathbb{D} : \kappa_h(\psi_h)). \quad (13)$$

Finally, we define two additional reconstructions which will be used to impose the Dirichlet boundary conditions. The reconstructions are written \mathfrak{R} and consist in a collection of cellwise nonconforming P^1 polynomials defined for all $c \in \mathcal{C}$ by

$$\begin{cases} \mathfrak{R}_c(v_h)(\mathbf{x}) := v_c + \mathcal{G}_c(v_h) \cdot (\mathbf{x} - \mathbf{x}_c), \\ \mathfrak{R}_c(\psi_h)(\mathbf{x}) := v_c + \mathcal{G}_c(\psi_h) \cdot (\mathbf{x} - \mathbf{x}_c). \end{cases} \quad (14)$$

where $\mathbf{x} \in c$ and \mathbf{x}_c is the barycentre of the cell c .

3.4 Mass bilinear form

In the DEM spirit, the reconstruction of functions is chosen as constant in each cell so as to obtain a diagonal mass matrix. The mass bilinear form is thus defined as

$$m_h((u_h, \varphi_h); (v_h, \psi_h)) := \sum_{c \in \mathcal{C}} \rho |c| (u_c \cdot v_c + (I \cdot \varphi_c) \cdot \psi_c). \quad (15)$$

3.5 Discrete problem

The discrete problem is defined as a lowest-order discontinuous Galerkin method similar to [12] and [10]. Consequently, penalty terms will be added to the discrete formulation of Equation (1) for two reasons. The first is that the gradient reconstruction of Equation (11) cannot by itself control (u_h, ϕ_h) and thus a least-square penalty term will be added to the formulation to ensure the well-posedness of the problem. More details can be found in [12] and [10]. The second is that the Dirichlet boundary conditions will not be imposed strongly but weakly through a least-squares penalty term acting on the boundary facet in $\partial\Omega_D$. Finally a consistency and a symmetry term are also added so as to ensure the consistency of the bilinear form as well as to conserve the symmetry of the discrete bilinear form.

3.5.1 Least-square penalty

For an interior facet $F \in \mathcal{F}^i$, writing $c_{F,-}$ and $c_{F,+}$ the two mesh cells sharing F , that is, $F = \partial c_{F,-} \cap \partial c_{F,+}$, and orienting F by the unit normal vector n_F pointing from $c_{F,-}$ to $c_{F,+}$, we define

$$[\mathfrak{R}(v_h)]_F := \mathfrak{R}_{c_{F,-}}(v_h) - \mathfrak{R}_{c_{F,+}}(v_h). \quad (16)$$

$[\mathfrak{R}(\psi_h)]_F$ is defined similarly. The interior penalty term is defined as

$$\begin{aligned} a_{\text{inner-pen}}((u_h, \varphi_h); (v_h, \psi_h)) := & \sum_{F \in \mathcal{F}^i} \frac{\eta}{h_F} \int_F ([\mathfrak{R}(u_h)]_F \otimes n_F) : \mathbb{C} : ([\mathfrak{R}(v_h)]_F \otimes n_F) \\ & + ([\mathfrak{R}(\varphi_h)]_F \otimes n_F) : \mathbb{D} : ([\mathfrak{R}(\psi_h)]_F \otimes n_F), \end{aligned} \quad (17)$$

where η is a penalty parameter whose value is determined experimentally in Section 3.7. For further inquiry, a lower bound on the penalty parameter η ensuring the stability of the numerical method can be found in [24]. The boundary penalty term is defined as

$$a_{\text{bnd-pen}}((u_h, \varphi_h); (v_h, \psi_h)) := \sum_{F \in \mathcal{F}_D^b} \frac{\eta}{h_F} \int_F ((G + G_c) \mathcal{R}_F(u_h) \cdot \mathcal{R}_F(v_h) + (M + M_c) \mathcal{R}_F(\varphi_h) \cdot \mathcal{R}_F(\psi_h)), \quad (18)$$

The corresponding linear form is defined to impose weakly the boundary conditions $u = u_D$ and $\varphi = \varphi_D$ on $\partial\Omega_D$:

$$l_D((v_h, \psi_h)) := \sum_{F \in \mathcal{F}_D^b} \frac{\eta}{h_F} \int_F ((G + G_c) u_D \cdot \mathcal{R}_F(v_h) + (M + M_c) \varphi_D \cdot \mathcal{R}_F(\psi_h)). \quad (19)$$

3.5.2 Symmetric Nitsche penalty

As the Dirichlet boundary conditions are imposed weakly, the discrete test functions do not verify $\mathcal{R}(v_h) = 0$ and $\mathcal{R}(\psi_h) = 0$ on $\partial\Omega_D$. Thus the following term, called consistency

term, coming from the integration by parts, leading from (4) to (7), must be taken into account

$$a_{\text{con}}((u_h, \varphi_h); (v_h, \psi_h)) := - \int_{\partial\Omega_D} (\sigma_h(u_h, \varphi_h) \cdot n) \cdot \mathcal{R}(v_h) + (\mu_h(\varphi_h) \cdot n) \cdot \mathcal{R}(\psi_h). \quad (20)$$

To keep the symmetry of the discrete bilinear form, the following symmetry term is defined

$$a_{\text{sym}}((u_h, \varphi_h); (v_h, \psi_h)) := - \int_{\partial\Omega_D} (\sigma_h(v_h, \psi_h) \cdot n) \cdot \mathcal{R}(u_h) + (\mu_h(\psi_h) \cdot n) \cdot \mathcal{R}(\varphi_h). \quad (21)$$

A corresponding linear form is added to compensate the term in (21) when the Dirichlet boundary conditions are verified exactly:

$$l_{\text{sym}}((u_h, \varphi_h); (v_h, \psi_h)) := - \int_{\partial\Omega_D} (\sigma_h(v_h, \psi_h) \cdot n) \cdot u_D + (\mu_h(\psi_h) \cdot n) \cdot \varphi_D. \quad (22)$$

3.5.3 Discrete problem

The bilinear form a_h is defined as $a_h := a_{\text{elas}} + a_{\text{inner_pen}} + a_{\text{bnd_pen}} + a_{\text{con}} + a_{\text{sym}}$. The discrete problem then writes: search for (u_h, φ_h) such that for all (v_h, ψ_h) , one has

$$m_h((u_h, v_h); (\varphi_h, \psi_h)) + a_h((u_h, v_h); (\varphi_h, \psi_h)) = l_h(v_h, \psi_h) + l_D(v_h, \psi_h) + l_{\text{sym}}(v_h, \psi_h), \quad (23)$$

where l_h is the linear form that takes into account Neumann boundary conditions and volumic loads and writes:

$$l_h(v_h, \psi_h) := \sum_{c \in \mathcal{C}} \left(\int_c f \right) \cdot v_c + \left(\int_c \mathfrak{c} \right) \cdot \psi_c + \sum_{F \in \mathcal{F}_N^b} \left(\int_F g \right) \cdot v_{c_F} + \left(\int_F m \right) \cdot \psi_{c_F}. \quad (24)$$

3.6 Interpretation as a DEM

The average value in an inner facet $F \in \mathcal{F}^i$ of a quantity a is defined as $\{a\}_F := \frac{1}{2}(a_{c_{F,-}} + a_{c_{F,+}})$. Rewriting Equation (13) and neglecting second order terms, one has

$$\begin{aligned} -a_{\text{elas}}((u_h, \varphi_h); (v_h, \psi_h)) &= \sum_{F \in \mathcal{F}^i} |F| (\{\sigma_h(u_h, \varphi_h)\}_F \cdot n_F) \cdot [v_h]_F \\ &+ \sum_{F \in \mathcal{F}^i} |F| (\{\mu_h(\varphi_h)\}_F \cdot n_F) \cdot [\psi_h]_F \\ &+ \sum_{c \in \mathcal{C}} |c| (\epsilon : \sigma_c(u_h, \varphi_h)) \cdot \psi_c \\ &+ \sum_{F \in \mathcal{F}^b} |F| (\sigma_{c_F}(u_h, \varphi_h) \cdot n_F) \cdot (v_{c_F} - \mathcal{R}_F(v_h)) \\ &+ \sum_{F \in \mathcal{F}^b} |F| (\mu_{c_F}(\varphi_h) \cdot n_F) \cdot (\psi_{c_F} - \mathcal{R}_F(\psi_h)) \\ &+ \mathcal{O}(h^2), \end{aligned} \quad (25)$$

where c_F designates the unique cell containing a boundary facet $F \in \mathcal{F}^b$, $\sigma_h(u_h, \varphi_h) := \mathbb{C} : e_h(u_h, \varphi_h)$, $\mu_h(\varphi_h) := \mathbb{D} : \kappa_h(\varphi_h)$ and for an inner facet F , $[v_h]_F := v_{c_{F,-}} - v_{c_{F,+}}$ and $[\psi_h]_F := \psi_{c_{F,-}} - \psi_{c_{F,+}}$. The principle of action-reaction (or Newton's third law) can be read in the first two equations through the action of jump terms. The third line represents the work of the momentum coming from the stresses. The fourth and fifth line represent the work of the internal forces and momenta but related to boundary facets. One can

write the dynamics equations of an interior cell $c \in \mathcal{C}$ (or discrete element), with no facet on the boundary, as follows

$$\begin{cases} \rho|c|\ddot{u}_c \simeq \sum_{F \in \mathcal{F}^i, F \subset \partial c} \iota_{c,F}|F|\{\sigma_h(u_h, \varphi_h)\}_F \cdot n_F + \int_c f, \\ \rho|c|I \cdot \ddot{\varphi}_c \simeq |c|\epsilon : \sigma_c(u_h, \varphi_h) + \sum_{F \in \mathcal{F}^i, F \subset \partial c} \iota_{c,F}|F|\{\mu_h(\varphi_h)\}_F \cdot n_F + \int_c \mathbf{c}, \end{cases} \quad (26)$$

up to second order terms and penalty terms and where $\iota_{c,F} = 1$ if $c = c_{F,-}$ and $\iota_{c,F} = -1$ if $c = c_{F,+}$. Each facet thus represents a link between two discrete elements and the forces and momenta are average quantities computed from cell-wise stress and momentum reconstructions. To obtain similar equations for a cell having a facet on $\partial\Omega$, one can refer to [18].

3.7 Validation test case

The domain considered is the square $\Omega = [-L, L]^2$, where $L = 0.5\text{m}$. The material parameters are $E = 1\text{Pa}$, $\nu = 0.3$ and $\ell = \frac{L}{2}$. Thus, classically $\lambda = \frac{E\nu}{(1-2\nu)(1+\nu)}$ and $G = \frac{E}{2(1+\nu)}$. We also take $G_c = G$ and $M = G\ell^2$. The manufactured solution considered for this test is

$$\begin{cases} u(x, y) = \frac{1}{2}(x^2 + y^2)(e_x + e_y), \\ \varphi(x, y) = (x - y), \end{cases} \quad (27)$$

where (x, y) is the current position in Ω and (e_x, e_y) is the Cartesian basis of Ω . The manufactured solution is imposed as Dirichlet boundary condition on the entire boundary $\partial\Omega$ and the associated volume loads f and \mathbf{c} are imposed in the volume:

$$\begin{cases} f(x, y) = -(\lambda + 2G)(e_x + e_y), \\ c(x, y) = 2G(x - y). \end{cases} \quad (28)$$

3.7.1 Fixing the penalty parameter

A structured mesh containing 6,400 triangles of uniform size $h = 0.025\text{m}$ is used for this test. The error with respect to the analytical solution will be determined depending on the values of the penalty parameter η appearing in (17), (18) and (19). Table 1 contains the computed errors. We choose $\eta = 10$ as it gives the lowest error on the gradients.

η	$\ (\nabla u, \nabla \varphi) - (\mathcal{G}_h(u_h), \mathcal{G}_h(\varphi_h))\ _{L^2}$
1	$2.35 \cdot 10^{-2}$
5	$1.74 \cdot 10^{-2}$
10	$1.62 \cdot 10^{-2}$
25	$1.67 \cdot 10^{-2}$
50	$1.72 \cdot 10^{-2}$
100	$1.80 \cdot 10^{-2}$

Table 1: Fixing the penalty parameter: value of penalty parameter and error in gradient norm.

3.7.2 Convergence rate

Structured triangular meshes are used for the convergence study. The mesh is refined uniformly. Table 2 presents the computed errors and estimated convergence rates. First

h	dofs	$\ (u, \varphi) - (\mathfrak{R}(u_h), \mathfrak{R}(\varphi_h))\ _{L^2}$	order	$\ (\nabla u, \nabla \varphi) - (\mathcal{G}_h(u_h), \mathcal{G}_h(\varphi_h))\ _{L^2}$	order
0.1	1,200	$2.55 \cdot 10^{-2}$	-	$6.80 \cdot 10^{-2}$	-
0.05	4,800	$1.27 \cdot 10^{-2}$	1.01	$3.12 \cdot 10^{-2}$	1.12
0.025	19,200	$6.37 \cdot 10^{-3}$	1.00	$1.62 \cdot 10^{-2}$	0.95
0.0125	76,800	$3.18 \cdot 10^{-3}$	1.00	$8.05 \cdot 10^{-3}$	1.01
0.00625	307,200	$1.59 \cdot 10^{-3}$	1.00	$4.01 \cdot 10^{-3}$	1.01

Table 2: Convergence rate: size of the mesh, number of dofs, L^2 -error and estimated order of convergence, error in gradient norm and estimated order of convergence.

order convergence in gradient norm and L^2 norm is observed.

4 Numerical results

First, two numerical tests in statics are presented and finally a numerical test in dynamics is presented.

4.1 Square plate with a hole

A square plate of length 100m has a hole of radius 10m in its center. For symmetry reasons, only a quarter of the plate is meshed. A traction with $T = 1$ s is imposed on the top surface. Figure 2 shows the boundary conditions. The material parameters are

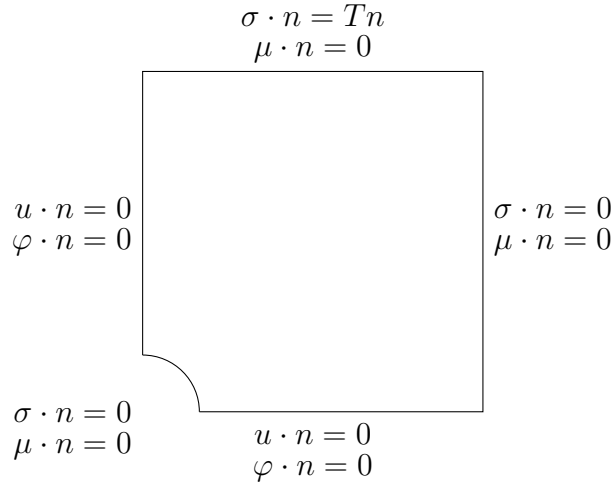


Figure 2: Square plate with a hole: problem setup.

as follows: $G = 10^3$ Pa, $\nu = 0.3$, $\ell = 0.2$ m and $G = G_c$. Three meshes are used for the computation from a coarse to a very fine one. The errors are computed with respect to a P^2 - P^1 Lagrange computation. Table 3 gives the computed errors. One can observe that the errors lower with the refinement of the meshes, as expected. Figures 3, 4 and 5 show respectively u_x , u_y and φ on the finest mesh for the two computations.

h	dofs FEM	dofs DEM	L^2 -error	gradient error
6.68	11,875	7,698	$1.634 \cdot 10^{-2}$	$1.840 \cdot 10^{-3}$
3.55	43,812	28,776	$5.895 \cdot 10^{-3}$	$8.659 \cdot 10^{-4}$
1.80	170,688	112,935	$1.703 \cdot 10^{-3}$	$3.829 \cdot 10^{-4}$

Table 3: Square plate with a hole: size of the mesh, number of dofs, L^2 -error and gradient error.

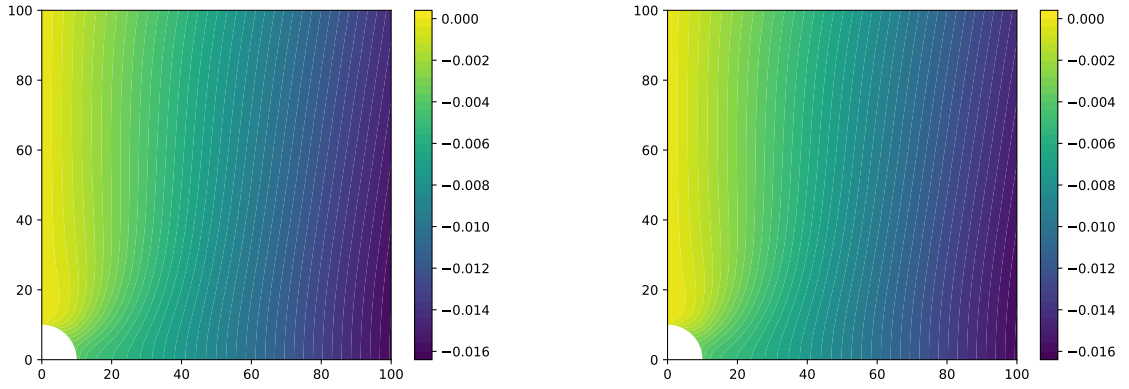


Figure 3: Plate with a hole: u_x . Left: DEM, right: FEM.

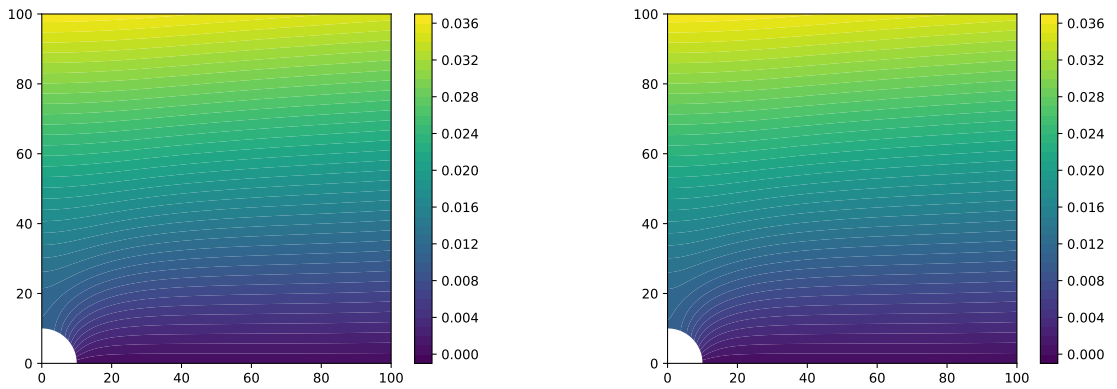
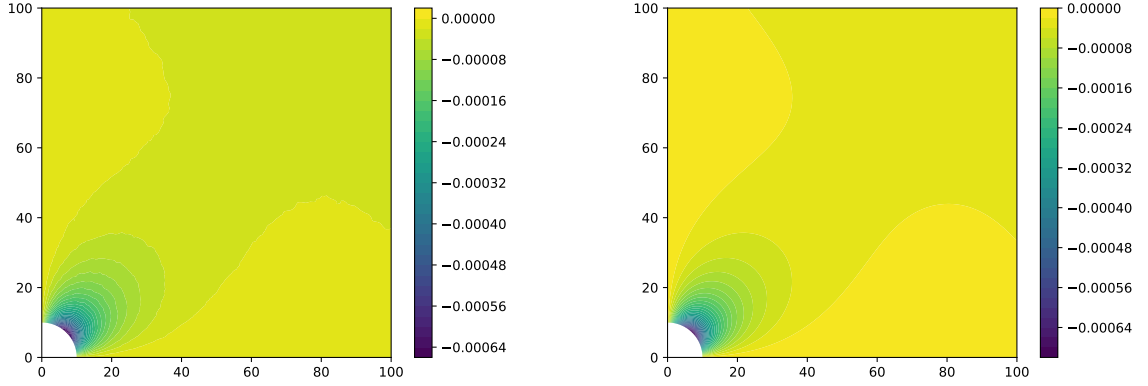


Figure 4: Plate with a hole: u_y . Left: DEM, right: FEM.

Figure 5: Plate with a hole: φ . Left: DEM, right: FEM.

4.2 Cube with a hole

A cube of length $L = 100\text{m}$ has a hole of radius $R = 10\text{m}$ in its center. For symmetry reasons, only an eighth of the cube is meshed. A traction T is imposed on the top surface. The exterior faces as well as the hole are stress free $\sigma \cdot n = 0$ and $\mu \cdot n = 0$. The interior faces are imposed mirror boundary conditions $u \cdot n = 0$ and $\varphi \cdot n = 0$. Figure 6 shows the boundary conditions. Two numerical experiments are considered for this test case. The

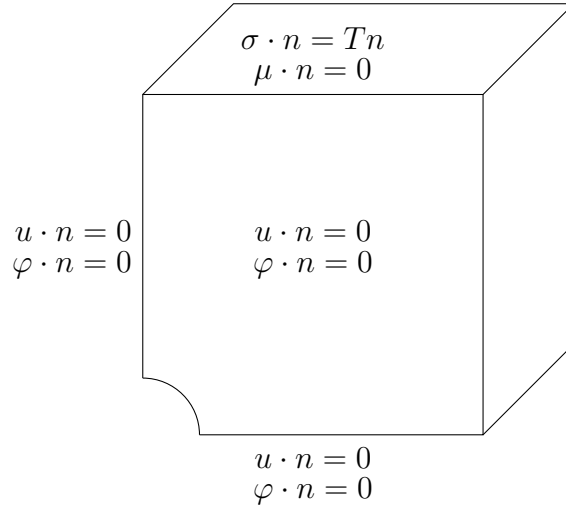


Figure 6: Cube with a hole: problem setup.

first with $\nu = 0.3$ and a P^2 - P^1 Lagrange computation is used as reference and the second where $\nu \rightarrow 0.5$ and the Lagrange computation fails.

4.2.1 Compressible material

The material parameters are $\nu = 0.3$, $G = 10 \cdot 10^6 \text{MPa}$, $G_c = 5 \cdot 10^6 \text{MPa}$, $\ell = 10\text{m}$ and $L = M = M_c = G\ell^2$. They were mainly taken from [28], with a few modifications. The traction stress is defined as $T = 1.0 \cdot 10^6 \text{Pa}$. An analytical solution for the stress concentration factor (SCF) from [20] is available. The reader is referred to [30] for details on the computation of the SCF. Table 4 gives the errors computed between the DEM

computation and the reference P^2 - P^1 Lagrange computation for a sequence of refined meshes as well as the error in the SCF. We observe the error between the two computations

h	dofs DEM	SCF error	dofs FEM	L^2 error	gradient error
59	3,078	34%	3,696	3.58	0.720
36	12,534	37%	13,116	3.36	0.643
22	68,142	12%	63,954	2.53	0.552
16	133,476	0.05%	121,272	1.96	0.458

Table 4: Cube with a hole: $\nu = 0.3$. Convergence of DEM computations: size of mesh, number of dofs in DEM computation, error in estimation of SCF, number of dofs in FEM computation, L^2 error and gradient error.

decreases when refining the mesh as expected. The error computed with the SCF also decreases when refining the mesh and leads to a very good approximation on the finest mesh.

4.2.2 Quasi-incompressible material

This numerical test is based on [30]. The material parameters are $\nu = 0.49$, $G = 1020\text{Pa}$, $G_c = 20\text{Pa}$, $M = 120\text{Pa}\cdot\text{m}^2$, $Mc = 80\text{Pa}\cdot\text{m}^2$ and $L = -6322\text{Pa}\cdot\text{m}^2$. Then, one computes $\lambda = \frac{2G\nu}{1-2\nu}$. Figure 7 shows a discrepancy in the vertical displacement between the two

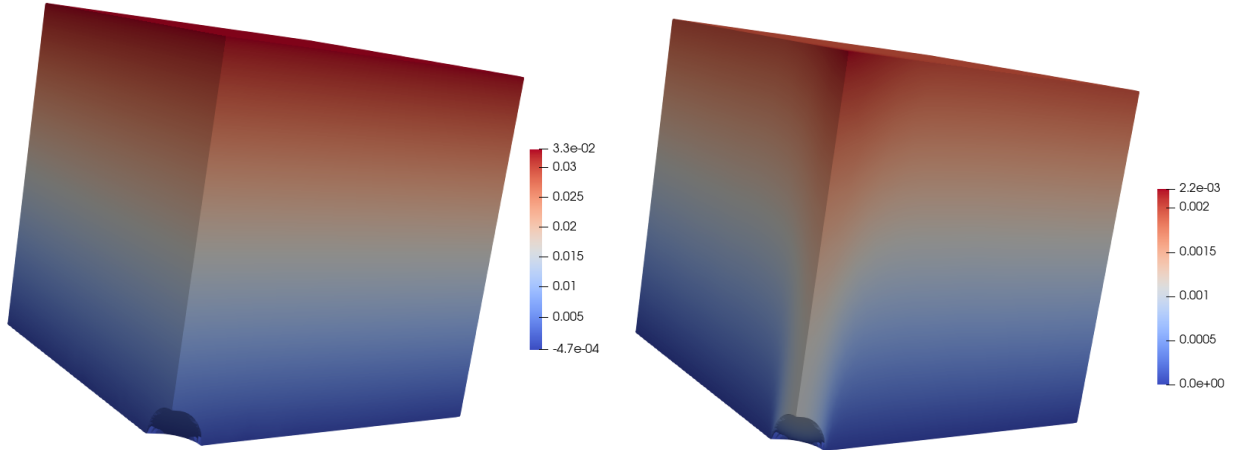


Figure 7: Cube with a hole: $\nu \rightarrow 0.5$. Left: $\Re(u_h) \cdot e_y$ DEM, right: u_y FEM.

computations: the FEM computation has a much lower displacement than the DEM computation. Figure 8 shows that the FEM computation clearly shows sign of locking when $\nu \rightarrow 0.5$ because we do not see a Poisson effect whereas the Poisson effect is very clear for the DEM computation.

4.3 Beam in dynamic flexion

This test case has been inspired by a similar from [6]. This test case consists in computing the oscillations of a beam of length $L = 1\text{m}$ with a rectangular section of $0.04 \times 0.1\text{m}^2$. The simulation time is $T = 0.5\text{s}$. The beam is clamped at one end, it is loaded by a

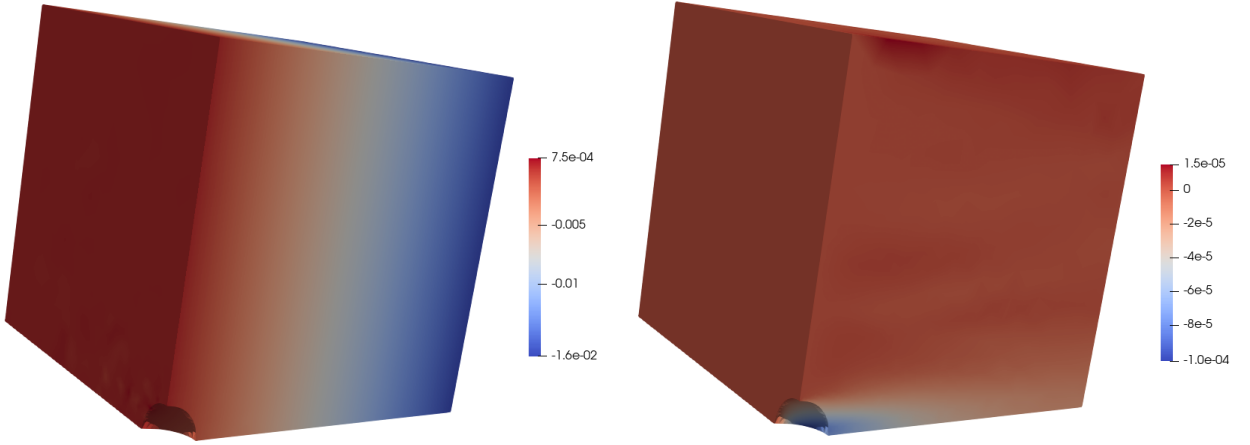


Figure 8: Cube with a hole: $\nu \rightarrow 0.5$. Left: $\mathfrak{R}(u_h) \cdot e_x$ DEM, right: u_x FEM.

uniform vertical traction $\sigma \cdot n = g(t)$ at the other end, and the four remaining lateral faces are stress free ($\sigma \cdot n = 0$ and $\mu \cdot n = 0$). The load term $g(t)$ is defined as

$$g(t) := \begin{cases} -\frac{5t}{2T}e_x & \text{for } 0 \leq t \leq \frac{2T}{5}, \\ 0 & \text{for } \frac{2T}{5} \leq t \leq T. \end{cases} \quad (29)$$

Figure 9 displays the problem setup. The material parameters are $E = 1\text{Pa}$ for the Young

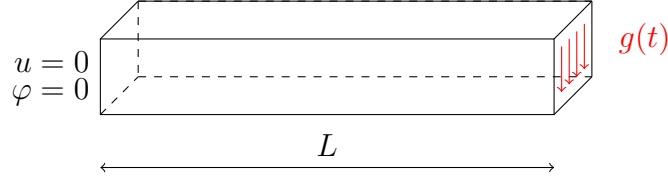


Figure 9: Beam in dynamic flexion: problem setup.

modulus and $\nu = 0.3$ for the Poisson ratio. The characteristic size of the microstructure is taken as $\ell = \frac{L}{10}$, so that we do not have $\ell \ll L$ in which case the Cosserat material can be homogenized in a Cauchy material [13]. We also take $Gc = \frac{G}{2}$ and $M = G\ell^2 = L = M_c$. The density is $\rho = 1\text{kg}\cdot\text{m}^{-3}$ and the inertia is taken as $I = \frac{2}{5}\ell^2$ following [28].

The reference solution is a P^2 - P^1 Lagrange FEM coupled to a Crank–Nicholson time-integration [5]. The DEM space discretization is coupled to a Leapfrog time-integration. The time-interval $(0, T)$ is discretized in $\{0 = t_0, \dots, t^n, \dots, t^N = T\}$. For all $n = 1, \dots, N$, we compute the discrete displacement and rotation u_h^n and φ_h^n and the discrete velocity $v_h^{n+\frac{1}{2}}$ and rotation rate $\psi_h^{n+\frac{1}{2}}$. The fully discrete scheme reads as follows: For all $n = 1, \dots, N$, given (u_h^n, φ_h^n) and $(v_h^{n+\frac{1}{2}}, \psi_h^{n+\frac{1}{2}})$, compute $(u_h^{n+1}, \varphi_h^{n+1})$ and $(v_h^{n+\frac{3}{2}}, \psi_h^{n+\frac{3}{2}})$ such that

$$\begin{cases} u_h^{n+1} = u_h^n + (t^{n+1} - t^n)v_h^{n+\frac{1}{2}} \\ \varphi_h^{n+1} = \varphi_h^n + (t^{n+1} - t^n)\psi_h^{n+\frac{1}{2}} \\ m_h((v_h^{n+\frac{3}{2}} - v_h^{n+\frac{1}{2}}, \psi_h^{n+\frac{3}{2}} - \psi_h^{n+\frac{1}{2}}); (\tilde{v}_h, \tilde{\psi}_h)) \\ = L_h(t^{n+1}; (\tilde{v}_h, \tilde{\psi}_h)) - a_h((u_h^{n+1}, \varphi_h^{n+1}); (\tilde{v}_h, \tilde{\psi}_h)), \quad \forall (\tilde{v}_h, \tilde{\psi}_h), \end{cases} \quad (30)$$

where m_h is defined in (15) and L_h is the discrete load linear form (the right-hand side of (23)). The initial displacement and rotation (u_h^0, φ_h^0) and the initial velocity and rotation rate $(v_h^{\frac{1}{2}}, \psi_h^{\frac{1}{2}})$ are evaluated by using the values of the prescribed initial displacement (u_0, φ_0) and the prescribed initial velocity (v_0, ψ_0) at the cell barycentres.

The time step is restricted by the following CFL stability condition:

$$\Delta t < 2\sqrt{\frac{\mu_{\min}}{\lambda_{\max}}}, \quad (31)$$

where μ_{\min} is the smallest entry of the diagonal mass matrix associated with the discrete mass bilinear form $m_h(\cdot, \cdot)$ and λ_{\max} is the largest eigenvalue of the stiffness matrix associated the discrete stiffness bilinear form $a_h(\cdot, \cdot)$. The CFL condition (31) guarantees the stability of the time-integration scheme.

A fine mesh is used for both computations. The DEM computation contains 108,000 dofs and the FEM computation 95,931 dofs. Figure 10 shows the displacement of the crack tip $u_h(L, 0.05, 0) \cdot e_y$ over $[0, T]$ for the two computations. Time-step is $\Delta t = 4.37 \cdot 10^{-7}$ s for the DEM computation whereas $\Delta t = 5 \cdot 10^{-3}$ s for the FEM computation. As expected,

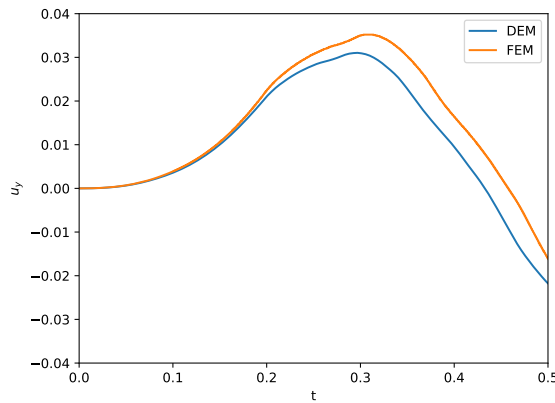


Figure 10: Beam in dynamic flexion: displacement of the tip of the beam over simulation time.

the two methods deliver similar results.

5 Conclusion

In this article, a variational DEM has been introduced which features only cell unknowns for the displacement and the micro-rotation. A cellwise gradient reconstruction is used to obtain cellwise constant strains and stresses using the formalism of Cosserat materials. An interpretation of the method as a DEM is presented in which the forces exerted by every facet (or link) between two cells (or discrete elements) are explicitly given as functions of the cellwise constant reconstructed stresses. Numerical tests have proved that the method converges at a similar rate as mixed Lagrange P^2 - P^1 FEM which is one in energy norm. Contrarily to FEM, the DEM has been shown to be robust with respect to the incompressible limit $\nu \rightarrow 0.5$.

Further work could include extending the present formalism to nonlinear material laws in small strains [28] and then finite strains [22]. It could also include computing nonlinear dynamic evolutions [23]. Also, the present formalism could be extended to Gyro-continua [7] to have a real rotation matrix in each cell.

Acknowledgements

The author would like to thank A. Ern from Inria and Ecole Nationale des Ponts et Chaussées for stimulating discussions and L. Monasse from Inria for carefully proof-reading this manuscript. The author would also like to thank K. Sab from Ecole Nationale des Ponts et Chaussées for sharing his knowledge regarding Cosserat continua.

References

- [1] D. André, J. Girardot, and C. Hubert. A novel DEM approach for modeling brittle elastic media based on distinct lattice spring model. *Computer Methods in Applied Mechanics and Engineering*, 350:100–122, 2019.
- [2] D. André, M. Jebahi, I. Iordanoff, J.-L. Charles, and J. Néauport. Using the discrete element method to simulate brittle fracture in the indentation of a silica glass with a blunt indenter. *Computer Methods in Applied Mechanics and Engineering*, 265:136–147, 2013.
- [3] D. Arnold. An interior penalty finite element method with discontinuous elements. *SIAM journal on numerical analysis*, 19(4):742–760, 1982.
- [4] B. Avci and P. Wriggers. A dem–fem coupling approach for the direct numerical simulation of 3d particulate flows. *Journal of Applied Mechanics*, 79(1), 2012.
- [5] T. Belytschko and T. J. R. Hughes. *Computational methods for transient analysis*, volume 1. Amsterdam, North-Holland(Computational Methods in Mechanics., 1983.
- [6] J. Bleyer. Numerical tours of computational mechanics with fenics. 2018.
- [7] M. Brocato and G. Capriz. Gyrocontinua. *International journal of solids and structures*, 38(6-7):1089–1103, 2001.
- [8] F. Cosserat, E. and Cosserat. *Théorie des corps déformables*. A. Hermann et fils, 1909.
- [9] P. Cundall and O. Strack. A discrete numerical model for granular assemblies. *geotechnique*, 29(1):47–65, 1979.
- [10] D. A. Di Pietro. Cell centered Galerkin methods for diffusive problems. *ESAIM: Mathematical Modelling and Numerical Analysis*, 46(1):111–144, 2012.
- [11] J.L. Ericksen. Liquid crystals and Cosserat surfaces. *The Quarterly Journal of Mechanics and Applied Mathematics*, 27(2):213–219, 1974.
- [12] R. Eymard, T. Gallouët, and R. Herbin. Discretization of heterogeneous and anisotropic diffusion problems on general nonconforming meshes SUSHI: a scheme using stabilization and hybrid interfaces. *IMA Journal of Numerical Analysis*, 30(4):1009–1043, 2009.
- [13] S. Forest, F. Pradel, and K. Sab. Asymptotic analysis of heterogeneous Cosserat media. *International Journal of Solids and Structures*, 38(26-27):4585–4608, 2001.

-
- [14] M. Godio, I. Stefanou, K. Sab, J. Sulem, and S. Sakji. A limit analysis approach based on Cosserat continuum for the evaluation of the in-plane strength of discrete media: application to masonry. *European Journal of Mechanics-A/Solids*, 66:168–192, 2017.
 - [15] W.G. Hoover, W.T. Ashurst, and R.J. Olness. Two-dimensional computer studies of crystal stability and fluid viscosity. *The Journal of Chemical Physics*, 60(10):4043–4047, 1974.
 - [16] M. Jebahi, D. André, I. Terreros, and I. Iordanoff. *Discrete element method to model 3D continuous materials*. John Wiley & Sons, 2015.
 - [17] J. Jeong and P. Neff. Existence, uniqueness and stability in linear Cosserat elasticity for weakest curvature conditions. *Mathematics and Mechanics of Solids*, 15(1):78–95, 2010.
 - [18] F. Marazzato, A. Ern, and L. Monasse. A variational discrete element method for quasistatic and dynamic elastoplasticity. *International Journal for Numerical Methods in Engineering*, 2020.
 - [19] Mark Michael, Frank Vogel, and Bernhard Peters. Dem–fem coupling simulations of the interactions between a tire tread and granular terrain. *Computer Methods in Applied Mechanics and Engineering*, 289:227–248, 2015.
 - [20] R. Mindlin and H. Tiersten. Effects of couple-stresses in linear elasticity. Technical report, COLUMBIA UNIV NEW YORK, 1962.
 - [21] L. Monasse and C. Mariotti. An energy-preserving discrete element method for elastodynamics. *ESAIM: Mathematical Modelling and Numerical Analysis*, 46:1527–1553, 2012.
 - [22] P. Neff. A finite-strain elastic–plastic Cosserat theory for polycrystals with grain rotations. *International Journal of Engineering Science*, 44(8-9):574–594, 2006.
 - [23] P. Neff and K. Chelminski. Well-posedness of dynamic Cosserat plasticity. *Applied Mathematics and Optimization*, 56(1):19–35, 2007.
 - [24] J. Nitsche. Über ein variationsprinzip zur lösung von dirichlet-problemen bei verwendung von teilträumen, die keinen randbedingungen unterworfen sind. *Abhandlungen aus dem Mathematischen Seminar der Universität Hamburg*, 36:9–15, 1971.
 - [25] H. Notsu and M. Kimura. Symmetry and positive definiteness of the tensor-valued spring constant derived from P1-FEM for the equations of linear elasticity. *Networks & Heterogeneous Media*, 9(4), 2014.
 - [26] D. Potyondy and P. Cundall. A bonded-particle model for rock. *International journal of rock mechanics and mining sciences*, 41(8):1329–1364, 2004.
 - [27] E. Providas and M.A. Kattis. Finite element method in plane Cosserat elasticity. *Computers & structures*, 80(27-30):2059–2069, 2002.
 - [28] H. Rattez, I. Stefanou, J. Sulem, M. Veveakis, and T. Poulet. Numerical analysis of strain localization in rocks with thermo-hydro-mechanical couplings using Cosserat continuum. *Rock Mechanics and Rock Engineering*, 51(10):3295–3311, 2018.
-

- [29] A. Ries, D. Wolf, and T. Unger. Shear zones in granular media: three-dimensional contact dynamics simulation. *Physical Review E*, 76(5):051301, 2007.
- [30] C. Sautot, S. Bordas, and J. Hale. Extension of 2d fenics implementation of Cosserat non-local elasticity to the 3d case. Technical report, Université du Luxembourg, 2014.
- [31] V.V. Shelukhin and M. Ružička. On Cosserat–bingham fluids. *ZAMM-Journal of Applied Mathematics and Mechanics/Zeitschrift für Angewandte Mathematik und Mechanik*, 93(1):57–72, 2013.
- [32] I. Stefanou, J. Sulem, and I. Vardoulakis. Three-dimensional Cosserat homogenization of masonry structures: elasticity. *Acta Geotechnica*, 3(1):71–83, 2008.